Infrared and Raman spectroscopic features of clinochlore Mg6Si4O10(OH)8: A density functional theory contribution

#Post-print of the article published in Applied Clay Science, 2020, 197, 105779, DOI
https://doi.org/10.1016/j.clay.2020.105779

Infrared and Raman spectroscopic features of Clinochlore $Mg_6Si_4O_{10}(OH)_8$: a Density Functional Theory contribution

Gianfranco Ulian, Daniele Moro and Giovanni Valdrè*

Centro di Ricerca Interdisciplinare di Biomineralogia, Cristallografia e Biomateriali
Dipartimento di Scienze Biologiche, Geologiche e Ambientali - Università di Bologna
Piazza di Porta San Donato 1, 40126 Bologna, Italy
**E-mail: giovanni.valdre@unibo.it*

Abstract

Mineral identification and analysis are often performed by using vibrational spectroscopies, namely infrared and Raman techniques. However, very few spectroscopy data are available on clinochlore, an important phyllosilicate with manifold applications in several fields. In the present work, *ab initio* Density Functional Theory simulation was employed to calculate the infrared and Raman spectra at Γ points and the phonon dispersion at different **k**-points of the magnesium end-member of clinochlore, with ideal chemical formula $Mg_6Si_4O_{10}(OH)_8$ and space group *C2/m*. Each phonon mode of the mineral was assigned to specific vibrations of the ionic groups in the structure. The theoretical results were found in good agreement with the available experimental data in literature, further extending the knowledge on the vibrational properties of clinochlore, which could be useful for experimental characterization of this mineral phase in various and different fields of research.

Keywords: Clinochlore, infrared and Raman spectroscopies, phonon dispersion relations, Density Functional Theory

1. Introduction

Clinochlore is a phyllosilicate mineral of the chlorite group whose ideal formula is $Mg_3^{IV'}Mg_3^{VI}Si_4^{IV}O_{10}(OH)_8$, composed by alternately stacked brucite-like (labelled as O') and talc-like (2:1 or TOT) layers (see Figure 1) held together by hydrogen bonds. According to conventional mineralogical rules, the superscripts VI′, VI, and IV refer to six-fold coordination of the octahedral interlayer cation, six-fold coordination of the TOT layer octahedral cation and the four-fold coordination of the tetrahedral cation, respectively (Bayliss, 1975; Wiewiora, 1990).

Clinochlore is an interesting clay mineral due to its peculiar surface properties. In fact, when cleaved, its surface often presents remainders of the O' layer above an intact TOT layer, resulting in a simultaneous exposition of regions related to the two layers. According to previous atomic force microscopy, Kelvin-probe force microscopy studies and quantum-mechanical simulations (Valdrè et al., 2011c; Valdrè et al., 2012; Moro et al., 2016; Moro et al., 2019a), the brucite-like layer is hydrophobic, whereas the 2:1 layer is hydrophilic, hence they present different features as adsorbents and/or catalysts. To cite some example, chlorite is able to adsorb, organize and self-assemble nucleotides, RNA and DNA (Valdrè, 2007; Valdrè et al., 2011a; Valdrè et al., 2011b), and amino acids, *e.g.* glycine and L-alanine (Moro et al., 2015; Moro et al., 2019b). The cited biomolecules were found selectively adsorbed on the brucite-like sheet and atomic force microscopy revealed different molecular conformations at the mineral surface. For example, RNA filaments adsorbed on atomic flat terraces were found as globular structures, whereas they were linearized on the edges of the brucite-like sheet (Valdrè et al., 2011b). DNA molecules were mainly found on the edges of the $Mg(OH)_6$ zones both in network-like and linear conformations and, in some cases, also as "bridges" between two parallel brucite-like stripes. In the case of amino acids, they were experimentally found as dot-like structures (single molecules), agglomerates and filament-like structures (Moro et al., 2015; Moro et al., 2019b). Very high adsorption energy between single molecules

and the brucite-like sheet was calculated from *ab initio* simulations, whose value was in the range 77 – 82 kJ/mol for glycine and 110 – 280 kJ/mol for L-alanine, depending on the local crystal-chemistry. The positive sign here indicates the energy necessary to desorb the molecule from the surface.

In addition zeolitic-type Brønsted-Lowry sites, which are known to control catalytic processes, were discovered on atomic flat surfaces (bi-dimensional systems) in chlorites and modelled by *ab initio* techniques (Valdrè et al., 2011c). For these reasons, there are many and various important applications of clinochlore (and clay minerals, in general) in several fields, from petrochemical refining, fine-chemical production, to water and air purification (Phuakkong et al., 2011; Stueckenschneider et al., 2014).

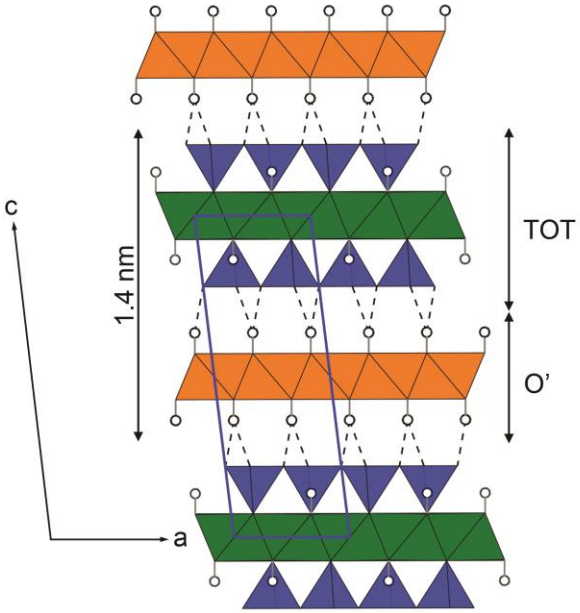

Figure 1. View along the **b**-axis of an ideal clinochlore mineral structure (s.g. *C*2/*m*). Talc-like (2:1, TOT) and brucite-like (O') structural units are indicated. Blue tetrahedrons represent the SiO_4, whereas orange and green octahedrons represent MgO_6 groups in the O' and TOT units, respectively. The blue solid line shows the crystallographic unit cell, whereas the dashed lines indicate the hydrogen bonds between the structural units.

One of the leading and simplest methods to investigate bulk structures and/or processes occurring at the surface is vibrational (infrared, IR or Raman) spectroscopy. For example, IR/Raman experiments are employed to recognize the presence of a mineral phase, by comparing the acquired spectrum with those available in databases (Fries and Steele, 2018), or to study fluid inclusions in minerals (Rosso and Bodnar, 1995). For surface processes, Attenuated Total Reflectance – Fourier Transform Infrared (ATR-FTIR) and confocal Raman spectroscopy are useful tools to investigate surfaces and reactions between minerals and the environment (*e.g.* molecules of gas/liquid) or intra-phase processes (King and Geisler, 2018). Very recently, infrared and Raman spectroscopy at the nanoscale, *i.e.* nano-FTIR, near-field FTIR and tip-enhanced Raman spectroscopy (TERS), are leading for promising applications and researches at the sub-micrometre level with very high resolution (Dominguez et al., 2014; Firkala et al., 2018; Bhattarai and El-Khoury, 2019; Kumar et al., 2019). The common factor between different applications is that a detailed knowledge of the vibrational modes of the mineral phase is required. For clinochlore, very few data on the infrared and Raman properties are available in literature (Gopal et al., 2004; Lafuente et al., 2016). In addition, the interpretation of experimental spectra is often difficult for several reasons, such as (1) the presence of impurities in both natural and synthetic samples, (2) the morphology of the samples (3) the presence of overtones and/or combination bands; (4) the impossibility to observe modes associated with weak intensities (low transition moments), (5) the availability only of poor crystalline samples, resulting in band broadening with extensive overlap of the signals, (6) polarization anisotropy in nano-FTIR and Raman and (7) residual strains in the minerals. In this perspective, *ab initio* quantum-mechanical simulations represent an effective tool to overcome the issues mentioned above, because they allow for the calculation of the phonon modes of solids. From the analysis of the vibrational motion of the atoms in the unit cell, it is also possible to successfully identify and assign to specific normal modes all of the fundamental vibrational transitions of the system in consideration, a task that is still very difficult by experimental means.

In the present work, a fundamental and detailed theoretical analysis of the infrared and Raman responses of monoclinic clinochlore (*C*2/*m* space group) is provided to fill the knowledge gap on this important clay mineral phase. The chemical composition here considered is that of an ideal, clinochlore end-member, where every T and M sites are occupied by silicon and magnesium, respectively. This monoclinic clinochlore model was geometrically optimized and its vibrational features at Γ point were investigated in detail using Density Functional Theory. Finally, the theoretical phonon dispersion relations of this mineral phase is reported and compared with the few data reported by Collins et al. (1993) on the acoustic phonons.

2. Theoretical methods

All the simulations related to the geometry optimization and the calculation of the phonon properties of clinochlore were performed within the Density Functional Theory (DFT) framework using the CRYSTAL17 periodic code (Dovesi et al., 2018), whereas graphical representations were carried out with the molecular graphics program VESTA (Momma and Izumi, 2011) and Moldraw (Ugliengo et al., 1993).

The chosen Hamiltonian was the hybrid B3LYP (Lee et al., 1988; Becke, 1993), where 20% of Hartree-Fock energy contributes to the DFT exchange term, because of its suitability for the *ab initio* investigations of vibrational properties of both molecular and solid (periodic) systems (Pascale et al., 2004; Pascale et al., 2005). The total energy (exchange/correlation) was evaluated on a pruned grid with 75 radial points and 974 angular points, subdivided in 5 intervals of 86, 194, 350, 974 and 350 points according to the Gauss-Legendre quadrature and Lebedev schemes (Prencipe et al., 2004). The thresholds controlling the accuracy of the calculation of the Coulomb and exchange integrals have been set to 10^{-8} (ITOL1 to ITOL4) and 10^{-16} (ITOL5); this means that when the overlap between two atomic orbitals is

lower than 10^{-ITOL}, the corresponding integral is either discarded or treated with less precision, as explained by Dovesi et al. (2018). The Hamiltonian matrix has been diagonalized through the Monkhorst and Pack scheme (Monkhorst and Pack, 1976), using a 6×6×2 k-mesh, which leads to 26 reciprocal lattice points (**k**-points). Weak intermolecular interactions, such as van der Waals forces, play a relevant role in determining the internal geometries of the crystal and its related properties. For this reason, a modified DFT-D2 scheme proposed by Grimme (2006) was employed to include those energy contributions to the final energy (Civalleri et al., 2008).

Within the Linear Combination of Atomic Orbitals (LCAO) approach, atomic and crystalline orbitals have been described by Gaussian-type orbitals basis sets. In particular, for magnesium and oxygen a 8-511d1G and a 8-411d11G (Valenzano et al., 2006; Ulian et al., 2016, 2018) basis sets were employed, respectively. Silicon and hydrogen were described by a 88-31G* (Nada et al., 1996; Ulian and Valdrè, 2015; Ulian et al., 2018) and a 3-1p1G basis sets (Gatti et al., 1994; Moro et al., 2015; Ulian et al., 2018), respectively. The chosen basis sets are well balanced, allowing accurate calculations in both molecular and crystal structures with sustainable computational costs.

The geometry of monoclinic clinochlore $Mg_6Si_4O_{10}(OH)_{10}$ (space group *C2/m*) was taken from the experimental refining of Welch and Marshall (2001) on a synthetic sample, which represents the closest structure to start with. All the simulations on this model were performed on the primitive cell, but structural results are referred to the crystallographic cell to ease the comparison (*vide infra*).

The cell parameters and internal coordinates of each model were optimized using the analytical gradient method for the atomic positions and a numerical gradient for the unit-cell parameters, to find the equilibrium geometry. The self-consistent field (SCF) procedure for the total energy calculations was considered converged when the energy difference between the last step and the previous one was less than 10^{-8} Ha during geometry optimization. The convergence on the structural optimization was reached when each component of the gradient was smaller than $3 \cdot 10^{-5}$ hartree $bohr^{-1}$ and displacements with

respect to the previous step were smaller than $12 \cdot 10^{-5}$ bohr. The Hessian matrix was upgraded with the Broyden-Fletcher-Goldfarb-Shanno (BFGS) algorithm. The structure parameters and atomic coordinates of the optimized clinochlore model (crystallographic cell) are reported in Table 1.

Table 1. Crystallographic cell structure (lattice parameters and atomic positions) of monoclinic stoichiometric clinochlore (s.g. *C2/m*), optimized at the Density Functional Theory/B3LYP-D* level, compared to experimental results.

B3LYP-D*					**Experimental (Welch and Marshall, 2001)**				
a	*b*	*c*	*β*	*V*	*a*	*b*	*c*	*β*	*V*
5.3297	9.2309	14.8947	96.829	727.590	5.332	9.224	14.414	97.07	703.52
Internal geometry					**Internal geometry**				
Atom	*x/a*	*y/b*	*z/c*	*Wyckoff*	*Atom*	*x/a*	*y/b*	*z/c*	*Wyckoff*
H1	0.2130	0.5000	0.1364	4i	H1	0.200	0.500	0.142	4i
H2	0.6204	0.5000	0.3639	4i	H2	0.117	0.320	0.358	4i
H3	0.1220	0.3338	0.3641	8j	H3	0.120	0.000	0.371	8j
Mg1	0.0000	0.0000	0.0000	2a	Mg1	0.000	0.000	0.000	2a
Mg2	0.5000	0.1663	0.0000	4g	Mg2	0.000	0.160	0.500	4g
Mg3	0.0000	0.3337	0.0000	4h	Mg3	0.000	0.353	0.000	4h
Mg4	0.0000	0.5000	0.5000	2d	Al4*	0.000	0.500	0.500	2d
O(a)	0.1910	0.1668	0.0739	8j	O1	0.185	0.172	0.080	8j
O(b)1	0.2136	0.0000	0.2209	4i	O2	0.228	0.000	0.234	4i
O(b)2	0.5029	0.2369	0.2210	8j	O3	0.509	0.220	0.231	8j
O(h)1	0.1907	0.5000	0.0715	4i	O4	0.181	0.500	0.068	4i
O(h)2	0.1424	0.0000	0.4283	4i	O5	0.168	0.000	0.435	4i
O(h)3	0.1432	0.3336	0.4285	8j	O6	0.135	0.337	0.430	8j
Si1	0.2277	0.1667	0.1844	8j	Si1†	0.224	0.166	0.193	8j

Notes: The experimental sample contained an Al-substitution in the O' layer (Al4 atom, marked with an asterisk) corresponding to the Mg4 atom in the simulated stoichiometric model and a partial substitution (25%) of silicon (Si1, marked with †) with aluminium.

There is an overall good agreement between the theoretical and experimental results of Welch and Marshall (2001), with the main difference residing in the **c**-axis length. Indeed, the synthetic Mg-rich clinochlore refined in the *C*2/*m* space group presented a chemical formula $(Mg_2Al)^{IV'}Mg_3{}^{VI}(AlSi_3)^{IV}O_{10}(OH)_8$, characterized by the following cation occupation: T = 0.25Al + 0.75Si, M1 = M2 = M3 = Mg, M4 = Al, whereas the simulated model has chemical composition $(Mg_3)^{IV'}Mg_3{}^{VI}(Si_4)^{IV}O_{10}(OH)_8$. The presence of some fraction of aluminium substitutions in both the tetrahedral sheet of the TOT layer and the O' layer increases the Coulomb (ionic) interactions between them, resulting in a lowered TOT – O' distance.

Harmonic phonon modes and vibrational frequencies were calculated at the Γ point on the optimized model of monoclinic clinochlore by diagonalizing the mass-weighted Hessian matrix (dynamical matrix), whose elements are the second derivatives of the lattice potential with respect to mass-weighted atomic displacements (Pascale et al., 2004). For these calculations, strict threshold criteria (10^{-10} Ha) were applied for the energy convergence to improve the accuracy of the vibrational results. Also, an anharmonic correction for OH stretching modes was applied, following the procedure described by Tosoni and co-workers (2005).

3. Results and discussion

Monoclinic, stoichiometric clinochlore $Mg_3(OH)_6Mg_3Si_4O_{10}(OH)_2$ (space group *C2/m*, point group C_{2h}) has a single unit formula per primitive unit cell (36 atoms). The phonon modes of this mineral phase are then 36 × 3 = 108, subdivided in three modes related to acoustic phonons (translations of the whole lattice) and 105 to optical ones. The presence of an inversion centre in the mineral leads to (1) vibrational modes active only in infrared or in Raman, but not in both (mutual exclusion rule), (2) the subdivision of the modes in *gerade* (labelled as *g*) and *ungerade* (*u*), namely vibrations that are symmetric or antisymmetric with respect to the inversion centre, respectively and (3) the absence of the longitudinal optical (LO) - transverse optical (TO) splitting. The LO-TO splitting is common in many layered silicates, in which atoms that vibrates perpendicularly to the layers (the so-called polar modes, or Fröhlich modes) should vibrate at their longitudinal optical frequency (Balan et al., 2001; Prencipe et al., 2009); however, the presence of the inversion centre nullify this effect (Prencipe et al., 2009).

The Γ-point vibrational modes can be classified according to the irreducible representation of the C_{2h} point group of the mineral as $\Gamma_{total} = \Gamma_{acoustic} + \Gamma_{optic} = 27A_g + 24A_u + 24\ B_g + 33A_u$ (Kroumova et al., 2003). The A_u and B_u modes are active in infrared spectroscopy, whereas A_g and B_g ones are Raman active. The three acoustic phonons are given by $A_u + 2B_u$ modes. A site symmetry analysis according to

Kroumova et al. (2003) is reported in Table 2. Each atom contributes to all active vibrational modes, Mg1 and Mg4 atoms in the trioctahedral sheet of the talc-like layer and of the brucite-like layer, respectively, are not associated with any *gerade* mode, which are those active in Raman spectroscopy.

Table 2. Site symmetry analysis for monoclinic clinochlore (s.g. *C2/m*).

Atom	*Layer*	*Wyckoff*	*Symmetry*
H1	TOT	4i	$2A_g + A_u + B_g + 2B_u$
H2	O'	4i	$2A_g + A_u + B_g + 2B_u$
H3	O'	8j	$3A_g + 3A_u + 3B_g + 3B_u$
Mg1	TOT	2a	$A_u + 2B_u$
Mg2	TOT	4g	$A_g + A_u + 2B_g + 2B_u$
Mg3	O'	4h	$A_g + A_u + 2B_g + 2B_u$
Mg4	O'	2d	$A_u + 2B_u$
O(a)	TOT	8j	$3A_g + 3A_u + 3B_g + 3B_u$
O(b)1	TOT	4i	$2A_g + A_u + B_g + 2B_u$
O(b)2	TOT	8j	$3A_g + 3A_u + 3B_g + 3B_u$
O(h)1	TOT	4i	$2A_g + A_u + B_g + 2B_u$
O(h)2	O'	4i	$2A_g + A_u + B_g + 2B_u$
O(h)3	O'	8j	$3A_g + 3A_u + 3B_g + 3B_u$
Si1	TOT	8j	$3A_g + 3A_u + 3B_g + 3B_u$
Total			$27A_g + 24A_u + 24B_g + 33B_u$

In Table 3, the calculated Γ-point frequencies of the transverse optical vibrational modes of monoclinic clinochlore, together with their transition moment corresponding to infrared and Raman activity are reported. The infrared spectrum of clinochlore was analytically calculated using the classical absorption formula as explained by Maschio et al. (2012):

$$A(\nu) = \frac{1}{3}\sum_{ii=1}^{3}\frac{4\pi}{\lambda\rho}\mathrm{Im}\left[n_{ii}(\nu)\right]$$

where $A(\nu)$ is the infrared absorption, λ if the wavelength of the incident light, ρ is the density of the mineral, n is the complex refractive index and ii represents the polarization direction. The real and imaginary parts of the refractive index n_{ii} were calculated as:

$$\left\{\mathrm{Re}\left[n_{ii}(\nu)\right]\right\}^2 - \left\{\mathrm{Im}\left[n_{ii}(\nu)\right]\right\}^2 = \mathrm{Re}\left[\varepsilon_{ii}(\nu)\right]$$

$$2\,\mathrm{Re}\left[n_{ii}(\nu)\right]\cdot\mathrm{Im}\left[n_{ii}(\nu)\right]=\mathrm{Im}\left[\varepsilon_{ii}(\nu)\right]$$

where $\varepsilon_{ii}(\nu)$ is the complex dielectric tensor, computed for each inequivalent polarization direction according to a classical Drude-Lorentz model:

$$\varepsilon_{ii}(\nu)=\varepsilon_{\infty,ii}+\sum_{p}\frac{f_{p,ii}\nu_p^2}{\nu_p^2-\nu^2-i\nu\gamma_p}.$$

In the previous equation, ε_∞ indicates the optical dielectric tensor, which was calculated using a couple-perturbed Kohn-Sham approach (Ferrero et al., 2008a; Ferrero et al., 2008b), whereas ν_p, f_p and γ_p are the transverse optical frequency, oscillator strength and damping factor of the p^{th} vibrational mode, respectively. The damping factor represents the full width at half maximum of each vibrational mode and was set to 8, which is a value that provides band broadening similar to that of experimental samples and also the default employed by CRYSTAL, as described by Maschio and co-workers (2012).

For what regards the Raman spectrum of clinochlore, it was calculated for a polycrystalline powder by using the transverse optical vibrational modes by means of a pseudo-Voigt functional form (Maschio et al., 2013a, b):

$$A(\nu)=\eta L(\nu)+(1-\eta)G(\nu)$$

where, in this case, $A(\nu)$ represents the Raman intensity and $L(\nu)$ and $G(\nu)$ are given by:

$$L(\nu)=\sum_{p}\frac{I_p}{\pi}\frac{\gamma_p/2}{\left(\nu-\nu_p\right)^2+\left(\gamma_p/2\right)^2}$$

$$G(\nu)=\sum_{p}2\sqrt{\frac{\ln 2}{\pi}}\frac{I_p}{\gamma_p}\exp\left[-\frac{4\ln 2\left(\nu-\nu_p\right)^2}{\gamma_p^2}\right]$$

198 with I_p the computed Raman intensities for the p^{th} vibrational mode and η is the Lorentz factor. A pure
199 Lorentzian form, which is the default of CRYSTAL (Maschio et al., 2013a), corresponding to $\eta = 1$, was
200 employed to obtain the typical sharp peaks of Raman spectra (Dovesi et al., 2018). The infrared and
201 Raman spectra for monoclinic clinochlore calculated as described above are reported in Figure 2a and
202 Figure 2b, respectively.

203

204

Table 3. Phonon frequencies (ν) and their irreducible representation (IRREP) of monoclinic clinochlore $Mg_3(OH)_6Mg_3Si_4O_{10}(OH)_2$ (s.g. C2/m) as obtained from Density Functional Theory simulations at the B3LYP-D* level. Amplitude is referred to transition moments in infrared (Ampl. IR) and Raman (Ampl. R).

Mode	ν (cm^{-1})	IRREP	Ampl. IR	Ampl. R	Mode	ν (cm^{-1})	IRREP	Ampl. IR	Ampl. R
1	0	B_u	0.0	0.0	55	450	A_u	596.0	0.0
2	0	B_u	0.0	0.0	56	454	B_u	1404.5	0.0
3	0	A_u	0.0	0.0	57	458	B_g	0.0	56.4
4	22	B_u	1.8	0.0	58	458	A_g	0.0	55.4
5	25	A_u	2.3	0.0	59	460	B_g	0.0	13.3
6	82	B_u	0.2	0.0	60	472	A_u	712.3	0.0
7	106	B_u	3.5	0.0	61	476	A_g	0.0	4.0
8	106	A_g	0.0	58.2	62	476	B_u	16.7	0.0
9	112	B_g	0.0	17.4	63	479	B_g	0.0	2.7
10	114	A_g	0.0	20.1	64	479	A_u	24.1	0.0
11	158	B_u	2.8	0.0	65	481	A_g	0.0	23.5
12	159	B_g	0.0	4.2	66	483	A_g	0.0	75.2
13	179	B_u	4.6	0.0	67	502	B_u	662.7	0.0
14	185	A_u	2.9	0.0	68	519	B_g	0.0	2.3
15	200	A_g	0.0	191.0	69	527	B_u	371.9	0.0
16	245	B_g	0.0	2.6	70	529	A_u	4.2	0.0
17	245	B_u	1.0	0.0	71	531	A_g	0.0	2.5
18	273	B_u	22.4	0.0	72	615	B_u	199.5	0.0
19	285	B_g	0.0	7.8	73	619	A_g	0.0	29.3
20	287	A_g	0.0	7.5	74	628	B_u	264.0	0.0
21	294	A_g	0.0	15.6	75	629	A_u	0.7	0.0
22	298	A_u	0.0	0.0	76	630	A_g	0.0	5.5
23	306	B_u	11.1	0.0	77	631	B_u	4.0	0.0
24	307	B_g	0.0	0.4	78	631	B_g	0.0	3.2
25	312	A_u	0.7	0.0	79	635	B_g	0.0	2.2
26	313	A_g	0.0	6.8	80	636	A_u	0.6	0.0
27	314	B_g	0.0	2.5	81	688	A_g	0.0	298.7
28	329	B_u	7.9	0.0	82	709	B_u	17.7	0.0
29	334	A_g	0.0	6.2	83	753	B_u	351.3	0.0
30	340	B_g	0.0	7.8	84	758	A_u	373.7	0.0
31	353	A_u	12.7	0.0	85	761	B_g	0.0	30.7
32	355	B_g	0.0	0.9	86	763	A_g	0.0	31.4
33	375	A_g	0.0	80.3	87	796	A_g	0.0	12.7
34	375	A_u	1.1	0.0	88	796	B_u	3.8	0.0
35	377	B_u	2.2	0.0	89	797	A_u	2.2	0.0
36	387	A_g	0.0	3.1	90	798	B_g	0.0	13.1
37	387	B_u	7.1	0.0	91	906	B_g	0.0	0.2
38	388	B_g	0.0	1.9	92	907	A_u	2.4	0.0
39	390	A_u	1.8	0.0	93	989	B_u	1945.4	0.0
40	390	B_g	0.0	0.1	94	1013	A_u	2672.1	0.0
41	392	A_g	0.0	11.3	95	1013	B_g	0.0	3.5
42	397	A_u	242.6	0.0	96	1013	B_u	2678.2	0.0
43	398	B_u	140.6	0.0	97	1013	A_g	0.0	3.5
44	400	B_u	515.4	0.0	98	1060	A_g	0.0	27.9
45	400	A_u	656.5	0.0	99	1092	B_g	0.0	0.0
46	403	B_g	0.0	0.4	100	1092	A_u	0.2	0.0
47	407	B_u	380.1	0.0	101†	3697	B_u	130.2	0.0
48	412	A_u	846.9	0.0	102†	3698	A_g	0.0	111.6
49	415	A_g	0.0	2.5	103†	3831	B_g	0.0	2.7
50	426	B_u	1730.2	0.0	104†	3831	A_u	4.9	0.0
51	431	A_u	1215.7	0.0	105†	3832	B_u	10.9	0.0
52	434	B_u	398.3	0.0	106†	3832	A_g	0.0	12.1
53	443	B_g	0.0	11.8	107†	3843	B_u	513.0	0.0
54	448	A_g	0.0	10.2	108†	3844	A_g	0.0	1000.0

Notes: modes 1 – 3 are acoustic phonons. IRREP is the irreproducible representation of the mode. Ampl.IR and Ampl.R are the calculated infrared and Raman transition amplitudes, respectively. Modes labelled with † are corrected for anharmonicity as of the model of Tosoni and co-workers (2005).

205

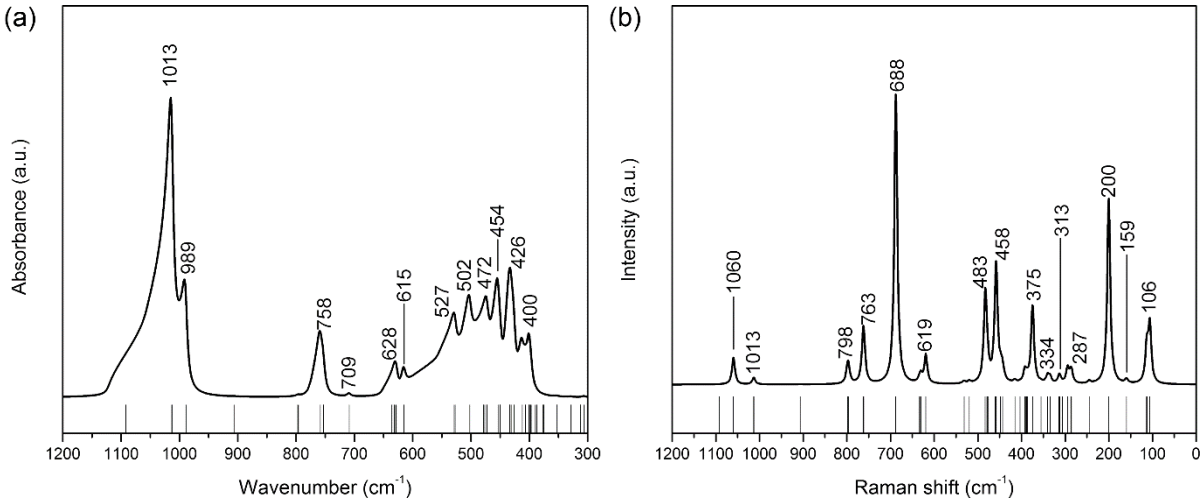

206

207 **Figure 2.** Simulated infrared (a) and Raman (b) spectra of monoclinic clinochlore

208 $Mg_3(OH)_6Mg_3Si_4O_{10}(OH)_2$ (space group *C2/m*).

209 Three regions were calculated in both the infrared and Raman spectra: a low-frequency region 0 – 500

210 cm^{-1}; an intermediate-frequency region between 500 and 1100 cm cm^{-1}; and a high-frequency region up

211 in the 3700 – 4000 cm^{-1}. The assignment of each normal mode was carried out by means of (1) graphical

212 animation of the atom motions using Moldraw (Ugliengo et al., 1993), (2) analysis of the vibrational

213 eigenvectors and of the potential energy distribution (PED), provided by CRYSTAL and (3) isotopic

214 substitutions, in particular $^{25}Mg \rightarrow {}^{24}Mg$, $^{29}Si \rightarrow {}^{28}Si$ and $^{2}D \rightarrow {}^{1}H$. CRYSTAL can easily calculate

215 isotopic shifts because the vibrational frequencies and normal modes are obtained from the

216 diagonalization of the mass-weighted dynamical matrix *W*, which is defined as:

217 $$W_{\alpha,\beta}(\mathbf{k}=0) = \frac{H}{\sqrt{M_\alpha M_\beta}}$$

218 where *H* is the dynamical matrix (matrix of the second-derivatives of the energy with respect to atom

219 displacements) and M_α and M_β are the masses of the atoms associated to the vibrational motion.

220 Vibrational isotopic shifts related to the $^{25}Mg \rightarrow {}^{24}Mg$, $^{29}Si \rightarrow {}^{28}Si$ substitutions are reported in Tables

4, whereas Table 5 shows those of the deuterium → hydrogen substitution. In the following, the results are discussed in details for the three spectral regions and compared to the available experimental results.

3.1. The 0–500 cm^{-1} region

In this region, 64 optic modes were computed, of which 33 are IR active (14 A_u + 19 B_u) and 31 are active in Raman (16 A_g + 15 B_g). Up to about 400 cm^{-1}, IR modes have very low intensity, which make them very difficult to observe experimentally. Even at theoretical level, the calculated amplitudes are very low. For the sake of an example, the analysis of the potential energy distribution revealed that the B_u mode at 106 cm^{-1} is related to a rotation of the Si – O(b) basal triangle, which is a mode with very low transition dipole moment in IR.

Below 400 cm^{-1}, Raman spectroscopy is more informative and sensitive. The weak band at 106 cm^{-1} is again related to the Si – O(b) triangle rotation as noted from IR. Two extremely weak signals were calculated at 112 and 114 cm^{-1}, which were assigned to bending modes of Si_2O_5 layers. The mode at 159 cm^{-1} was related, instead, to a combination of the out-of-plane vibration of the magnesium ions and to librations of the OH groups in the brucite-like interlayer. There is a quite intense peak at 200 cm^{-1} related to a symmetric MgO_6 vibration that moves also the T sheets along the **c**-axis direction. These results are in good agreement with the experimental observations of Rinaudo et al. (2004) on phlogopite, where these signals were measured at 102, 120, 153 and 195 cm^{-1}. The only exception is the assignment of the mode at 102 cm^{-1}, which the authors correlated to MO_6 vibrations. Three very weak bands were observed at 334, 313 and 287 cm^{-1}, which were assigned to Si – O(b) – Si bending, Mg – O(h) – Mg bending in the brucite-like layer and Si – O(b) – Si bending, respectively. A weak band at 375 cm^{-1} is related to a Mg – O(h) – Mg bending mode of the TOT layer. Finally, the peaks in the Raman spectrum at 458 cm^{-1}

and 483 cm^{-1} are related to two modes of the O' layer, namely OH librations and Mg – O(h) – Mg bending, respectively.

Above 400 cm^{-1}, quantum mechanical simulations of the infrared spectrum of clinochlore provided vibrational signals with higher intensities (about 100 times those below 400 cm^{-1}). Between 500 and 600 cm^{-1}, the spectrum is mainly due to octahedral MgO_6 modes. The first peak (400 cm^{-1}) is given by two optic modes related to Mg – O(h) – Mg bending mode of the TOT layer, one showing Mg displacement normal to the layer and the second with Mg motion parallel to the (001) plane. There are two strong signals at 426 cm^{-1} and 431 cm^{-1} related to OH librations (Mg – O(h) – H bending) in the O' layer, normal to [001]. An MgO_6 deformation parallel to the (001) plane and associated with O(b) – Si – O(b) bending was calculated at 434 cm^{-1}, whereas two overlapping modes at 450 cm^{-1} (1/4 of the intensity of highest signal) and 454 cm^{-1} (1/2 of the intensity of highest signal) showed similar Mg-centred motions together with O(b) – Si – O(a) bending. At 472 cm^{-1}, collective O – Mg – O bending modes in both the TOT and O' layers were calculated, whereas two very weak signals at 476 and 479 cm^{-1}, hidden below the previous one, were mainly due to Mg motions in the brucite-like layer. MgO_6 stretching modes in association with O(b) – Si – O(a) bending in the TOT layer were calculated at 502 cm^{-1} (medium intensity, 1/4 of the highest signal) and 527 cm^{-1} (medium to low intensity, 1/7 of the highest signal).

Making a comparison with the experimental results by Gopal et al. (2004), it is interesting to note that this region presents a single, strong signal centred between 435 – 450 cm^{-1}, with many shoulders and small sub-peaks, which are overall in good agreement with the present theoretical simulation. The small discrepancies are mainly due to the aluminium substitutions in both the TOT layer (Al^{3+}/Si^{4+} substitutions) and the O' layer (Al^{3+}/Mg^{2+} substitutions) that are a common feature of real samples and also affects the mineral structure (Gopal et al., 2004; Valdrè et al., 2009; Moro et al., 2016; Moro et al., 2019a; Moro et al., 2019b). The different crystal-chemistry not only affects, for example, the unit cell

structure (*e.g.* the larger **c**-axis parameter in Table 1) or the elastic properties of the mineral (Ulian et al., 2018), but also the chemical environment of the anionic/cationic groups, and IR/Raman spectroscopies are very sensitive to these variations. Also, it is important to stress that in the low-frequency region the modes are expected to be affected by an extremely limited anharmonicity, probably smaller than 3–4 cm^{-1}, as also discussed by Prencipe et al. (2009) for lizardite.

3.2. The 500–1100 cm^{-1} region

The theoretical analysis revealed 33 optical modes in this region, whereas few and very broad peaks were experimentally observed in both IR and Raman spectroscopies. Gopal et al. (2004) reported an infrared signal at 653 cm^{-1} that was assigned to M – OH libration. The same signal calculated at the B3LYP-D* level is at 758 cm^{-1}, given by two modes at 753 and 758 cm^{-1}. This high discrepancy is due to the anharmonic behaviour of this kind of modes for which the CRYSTAL code does not provide a correction. Indeed, while the O – H stretching modes are usually uncoupled with other vibrational modes and a reliable correction for anharmonicity was implemented in CRYSTAL by Tosoni et al. (2005), in the case of H-bending modes such a correction is not applicable due to the coupling with other modes having similar frequencies (Prencipe et al., 2009). Very recently, a computational approach based on the vibrational configuration interaction method was proposed by Erba and co-workers (Erba et al., 2019a; Erba et al., 2019b) to explicitly calculate the phonon-phonon coupling and evaluate the anharmonic vibrational states of solids. However, this method is not available in version of the CRYSTAL code here employed and, in addition, would demand high computational requirements for complex phases such as layered silicates (Erba et al., 2019a; Erba et al., 2019b).

The present Density Functional Theory simulations provided also two very small IR peaks at 615 and 628 cm^{-1} that were attributed to OH librations in the brucite-like layer. Given the previous consideration,

these signals are affected by anharmonicity and their position in real spectra should be considered with care.

An asymmetric SiO_4 umbrella bending was calculated at 709 cm^{-1} in the infrared spectrum, but this mode has an extremely low intensity and it could not be observable by experimental equipment or could appear as a shoulder on the OH libration band. The symmetric counterpart, which is Raman active, was calculated at 688 cm^{-1}, and it is the signal with highest intensity in the 0 – 1100 cm^{-1} spectral region.

The asymmetric Si – O(a) and Si – O(b) stretching modes were calculated at 989 (one mode) and 1013 cm^{-1} (two modes) in the infrared spectrum, which are in good agreement with the experimentally measured values of 958 and 998 cm^{-1} reported by Gopal et al. (2004). Another Si – O(b) stretching mode was calculated at 1092 cm^{-1}, appearing as a shoulder of the more intense Si – O(b) vibration. The Raman spectrum contained the symmetric Si – O modes, with two Si – O(b) vibrations overlapping at about 1015 cm^{-1} and one Si – O(a) stretching mode at 1060 cm^{-1}. At 906 cm^{-1} an asymmetric Si – O(a) was calculated in the Raman spectrum, but it presented almost zero intensity (1/5000 of the most intense peak).

Table 4. Calculated isotopic shifts (cm^{-1}) according to the $^{25}Mg \rightarrow {}^{24}Mg$ and $^{29}Si \rightarrow {}^{28}Si$ substitutions (see paragraph 3 for details).

ν (cm^{-1})	IRREP	Isotopic shift					ν (cm^{-1})	IRREP	Isotopic shift				
		Mg1	*Mg2*	*Mg3*	*Mg4*	*Si*			*Mg1*	*Mg2*	*Mg3*	*Mg4*	*Si*
22	B_u	0.0	0.0	-0.1	0.0	0.0	431	B_u	0.0	-1.5	0.0	0.0	-0.2
25	A_u	0.0	0.0	-0.1	0.0	0.0	443	B_g	0.0	-3.1	0.0	0.0	-1.5
82	B_u	0.0	-0.1	-0.3	-0.1	-0.1	448	A_g	0.0	-3.6	0.0	0.0	-0.8
106	B_u	0.0	0.0	0.0	0.0	0.0	450	A_u	-1.7	-2.7	0.0	0.0	-1.4
106	A_g	0.0	0.0	0.0	0.0	0.0	454	B_u	-0.1	-0.6	0.0	0.0	-1.1
112	B_g	0.0	0.0	0.0	0.0	-0.9	458	B_g	0.0	0.0	-0.1	0.0	0.0
114	A_g	0.0	0.0	0.0	0.0	-0.9	458	A_g	0.0	-0.1	-0.1	0.0	-0.1
158	B_u	0.0	0.0	-0.7	-1.4	0.0	460	B_g	0.0	-2.6	0.0	0.0	-1.1
159	B_g	0.0	0.0	-2.1	0.0	0.0	472	A_u	-0.9	-0.1	-0.1	-0.3	-1.1
179	B_u	-0.5	-0.8	0.0	0.0	-0.5	476	A_g	0.0	0.0	-5.1	0.0	0.0
185	A_u	-0.4	-0.9	0.0	0.0	-0.5	476	B_u	0.0	0.0	-1.8	-3.4	0.0
200	A_g	0.0	0.0	0.0	0.0	-1.4	479	B_g	0.0	0.0	-5.2	0.0	0.0
245	B_g	-1.5	-2.4	0.0	0.0	-0.3	479	A_u	0.0	0.0	-1.6	-3.3	0.0
245	B_u	0.0	-0.5	0.0	0.0	-0.3	481	A_g	0.0	-1.4	0.0	0.0	-0.4
273	B_u	-0.3	-1.2	0.0	0.0	-0.4	483	A_g	0.0	0.0	-0.1	0.0	0.0
285	B_g	0.0	0.0	0.0	0.0	0.0	502	B_u	-1.5	-1.6	-0.3	-0.2	-0.1
287	A_g	0.0	0.0	0.0	0.0	0.0	519	B_g	0.0	-0.1	0.0	0.0	-0.3
294	A_g	0.0	0.0	0.0	0.0	-0.5	527	B_u	-0.5	-0.5	-0.2	-0.1	-0.2
298	A_u	-0.1	0.0	0.0	0.0	-0.4	529	A_u	0.0	0.0	0.0	0.0	-0.1
306	B_u	-0.2	0.0	-0.1	-0.1	0.0	531	A_g	0.0	-0.1	0.0	0.0	-0.1
307	B_g	0.0	-1.1	-0.1	0.0	-0.1	615	B_u	-0.2	-0.5	-1.3	-0.5	-0.1
312	A_u	0.0	-0.1	0.0	-0.1	-0.4	619	A_g	0.0	0.0	0.0	0.0	0.0
313	A_g	0.0	0.0	-0.2	0.0	-0.1	628	B_u	-0.1	-0.3	-3.2	-1.8	-0.1
314	B_g	0.0	-0.4	-0.1	0.0	-0.3	629	A_u	0.0	0.0	0.0	0.0	-0.3
329	B_u	-2.1	-0.7	0.0	0.0	-0.3	630	A_g	0.0	0.0	0.0	0.0	-0.3
334	A_g	0.0	0.0	0.0	0.0	-0.1	631	B_u	0.0	0.0	-0.1	-0.5	-0.3
340	B_g	0.0	-1.4	0.0	0.0	-0.5	631	B_g	0.0	0.0	-0.7	0.0	-0.2
353	A_u	-2.0	-0.5	0.0	-0.1	-2.6	635	B_g	0.0	0.0	-0.4	0.0	-0.2
355	B_g	0.0	-2.4	-0.1	0.0	-2.3	636	A_u	0.0	0.0	0.0	0.0	-0.2
375	A_g	0.0	-1.1	0.0	0.0	-0.2	688	A_g	0.0	0.0	0.0	0.0	-2.2
375	A_u	-0.2	-1.3	0.0	0.0	-0.8	709	B_u	-0.8	-1.5	-0.1	0.0	-2.7
377	B_u	-0.9	-0.8	0.0	-0.1	-0.7	753	B_u	-0.1	0.0	0.0	0.0	-1.1
387	A_g	0.0	-0.1	-3.3	0.0	0.0	758	A_u	0.0	0.0	0.0	0.0	-0.9
387	B_u	0.0	0.0	-1.1	-2.7	0.0	761	B_g	0.0	-0.2	0.0	0.0	-1.5
388	B_g	0.0	-0.9	-1.8	0.0	-0.8	763	A_g	0.0	0.0	0.0	0.0	-1.4
390	A_u	-0.1	0.0	-2.1	-2.0	0.0	796	A_g	0.0	0.0	0.0	0.0	-10.6
390	B_g	0.0	-0.1	-1.5	0.0	0.0	796	B_u	0.0	0.0	0.0	0.0	-11.0
392	A_g	0.0	-2.2	-0.1	0.0	-0.7	797	A_u	0.0	0.0	0.0	0.0	-11.2
397	A_u	0.0	0.0	-1.6	-1.5	0.0	798	B_g	0.0	-0.1	0.0	0.0	-10.6
398	B_u	0.0	-1.3	-2.1	-1.2	0.0	906	B_g	0.0	0.0	0.0	0.0	-4.1
400	B_u	-1.8	-1.8	0.0	0.0	-0.1	907	A_u	0.0	0.0	0.0	0.0	-4.1
400	A_u	-0.7	-0.5	0.0	0.0	-0.4	989	B_u	0.0	-0.1	-0.1	-0.1	-6.5
403	B_g	0.0	0.0	-2.3	0.0	0.0	1013	A_u	0.0	0.0	0.0	0.0	-4.6
407	B_u	0.0	0.0	-1.6	-1.5	0.0	1013	B_g	0.0	0.0	0.0	0.0	-4.6
412	A_u	0.0	0.0	-0.6	-0.2	0.0	1013	B_u	0.0	0.0	0.0	0.0	-4.6
415	A_g	0.0	0.0	0.0	0.0	0.0	1013	A_g	0.0	0.0	0.0	0.0	-4.6
426	B_u	-0.2	0.0	-0.2	-0.1	0.0	1060	A_g	0.0	0.0	0.0	0.0	-7.6
434	A_u	-4.7	0.0	-0.1	-0.1	0.0	1092	B_g	0.0	0.0	0.0	0.0	-1.6

305

Table 5. Calculated isotopic shifts (cm^{-1}) according to the $^2D \rightarrow {}^1H$ substitutions (see paragraph 3 for details).

ν (cm^{-1})	IRREP	Isotopic shift			ν (cm^{-1})	IRREP	Isotopic shift		
		H1	*H2*	*H3*			*H1*	*H2*	*H3*
0	B_u	0.0	0.0	0.0	450	A_u	-4.3	-0.3	-1.7
0	B_u	0.0	0.0	0.0	454	B_u	-13.9	0.0	-0.6
0	A_u	0.0	0.0	0.0	458	B_g	-3.2	-14.1	-14.7
22	B_u	0.0	-0.1	-0.1	458	A_g	-0.2	-10.0	-10.0
25	A_u	0.0	0.0	-0.1	460	B_g	-2.6	0.0	-3.2
82	B_u	-0.1	-0.3	-0.6	472	A_u	-14.1	-0.4	-4.4
106	B_u	0.0	0.0	0.0	476	A_g	-9.5	-3.2	-10.6
106	A_g	0.0	0.0	0.0	476	B_u	0.0	-2.4	-9.2
112	B_g	0.0	-0.1	0.0	479	B_g	0.0	-1.6	-7.4
114	A_g	0.0	0.0	0.0	479	A_u	-0.1	-0.1	-5.0
158	B_u	0.0	-6.4	-8.9	481	A_g	-5.0	-2.0	-5.7
159	B_g	0.0	-3.9	-11.3	483	A_g	0.0	-2.2	-2.2
179	B_u	-1.0	0.0	0.0	502	B_u	-2.6	-0.1	-5.8
185	A_u	-0.3	0.0	-0.1	519	B_g	-1.0	-0.4	-15.7
200	A_g	-0.2	0.0	0.0	527	B_u	-2.7	-0.8	-22.9
245	B_g	-2.6	-0.1	-0.1	529	A_u	-0.2	0.0	-29.5
245	B_u	-1.4	0.0	-0.3	531	A_g	-0.7	-0.1	-35.8
273	B_u	-5.0	0.0	0.0	615	B_u	-38.4	-52.9	-86.8
285	B_g	0.0	-0.3	-0.3	619	A_g	-41.5	-53.1	-87.8
287	A_g	0.0	-1.0	-0.1	628	B_u	-13.7	-7.9	-41.5
294	A_g	-0.9	-5.2	-3.0	629	A_u	-54.2	-86.7	-100.5
298	A_u	-0.2	-1.7	-12.8	630	A_g	-11.1	-4.4	-45.6
306	B_u	-0.2	-8.6	-15.8	631	B_u	-3.3	-2.5	-10.0
307	B_g	-3.3	-3.7	-11.4	631	B_g	-49.7	-76.3	-111.8
312	A_u	-0.1	-5.2	-7.2	635	B_g	-3.1	0.0	-24.5
313	A_g	-0.6	-6.1	-10.5	636	A_u	-5.7	-0.1	-31.9
314	B_g	-1.6	-2.1	-3.8	688	A_g	-56.5	-0.2	-0.2
329	B_u	-2.7	-1.6	-0.3	709	B_u	-76.8	-0.2	-0.4
334	A_g	-2.4	-0.2	-0.5	753	B_u	-44.6	-0.2	-0.5
340	B_g	-0.1	0.0	-1.6	758	A_u	-122.4	-0.1	-0.4
353	A_u	0.0	-3.2	-36.1	761	B_g	-125.8	-0.2	-0.4
355	B_g	0.0	-1.2	-8.1	763	A_g	-75.1	-0.3	-0.5
375	A_g	-7.1	-20.6	-23.5	796	A_g	-2.3	-1.1	-1.5
375	A_u	-2.3	-15.4	-24.1	796	B_u	-2.3	-0.9	-1.4
377	B_u	-1.9	-25.9	-45.9	797	A_u	-1.7	-0.9	-1.9
387	A_g	-0.1	-11.9	-14.7	798	B_g	-2.7	-0.6	-1.8
387	B_u	0.0	-10.2	-10.3	906	B_g	-0.5	-0.1	-0.3
388	B_g	-0.3	-11.5	-32.9	907	A_u	-0.5	-0.1	-0.3
390	A_u	0.0	-14.3	-16.8	989	B_u	-0.1	-0.2	-0.4
390	B_g	0.0	-1.4	-7.5	1013	A_u	-0.1	0.0	0.0
392	A_g	-0.7	-2.8	-15.5	1013	B_g	-0.1	0.0	0.0
397	A_u	-1.5	-6.7	-14.3	1013	B_u	-0.1	0.0	0.0
398	B_u	-1.2	-10.9	-17.5	1013	A_g	-0.1	0.0	0.0
400	B_u	-1.8	0.0	-0.3	1060	A_g	-0.2	0.0	0.0
400	A_u	-3.5	0.0	0.0	1092	B_g	0.0	-0.1	-0.1
403	B_g	0.0	-2.6	-14.6	1092	A_u	0.0	-0.1	-0.1
407	B_u	0.0	-0.1	-6.3	3849	B_u	-1037.0	0.0	0.0
412	A_u	0.0	-7.2	-9.5	3850	A_g	-1036.4	0.0	0.0
415	A_g	0.0	-21.3	-22.3	3975	B_g	0.0	0.0	-1074.9
426	B_u	0.0	-17.7	-18.8	3975	A_u	0.0	0.0	-1074.9
434	A_u	-0.1	-17.7	-20.5	3976	B_u	0.0	-1072.5	4.7
431	B_u	-0.7	-0.2	-0.1	3976	A_g	0.0	-1071.7	5.0
443	B_g	-12.3	-37.4	-38.7	3987	B_u	0.0	-4.7	-1082.8
448	A_g	-11.0	-19.3	-44.6	3988	A_g	0.0	-4.9	-1081.9

3.3. The 3700–4000 cm^{-1} region.

This is the region dominated by the hydroxyl stretching modes of both the talc-like and the brucite-like layer. Here, 8 optical modes were computed, four IR-active ($A_u + 3B_u$) and four active in Raman spectroscopy ($3A_g + B_g$). Within the harmonic approximation, the calculated vibrational frequency of the infrared OH-modes were 3849 cm^{-1}, 3975 cm^{-1}, 3976 cm^{-1} and 3987 cm^{-1}, whereas the frequencies of Raman-active modes were 3850 cm^{-1}, 3975 cm^{-1}, 3976 cm^{-1} and 3988 cm^{-1}. As reported in Table 2, the anharmonic constant for these modes is quite remarkable, of about 150 cm^{-1}, in agreement with previous theoretical observations (Tosoni et al., 2005; Prencipe et al., 2009). This is a well-known issue related to the very low mass of hydrogen, whose vibrational displacement is often large, whereas the assumption of harmonic oscillators requires small nuclear movements. For this means, the correction proposed by Tosoni and co-workers (2005), which is based on a numerical solution of the Schrödinger equation along the O – H coordinate for fully decoupled hydroxyl stretching modes, was employed. The interested readers can find further details in the work of Tosoni et al. (2005).

By considering the anharmonic vibrational frequencies, the first two lines (101, B_u and 102, A_g) reported in Table 2, centred at about 3700 cm^{-1}, were related to OH stretching modes of the TOT layer, whereas the other six vibrations at higher frequencies (3830 – 3850 cm^{-1}) are due to O – H vibrations in the O' layer. These figures are quite different from those experimentally measured by Gopal et al. (2004), who reported these signals between 3438 cm^{-1} and 3678 cm^{-1}, and can be explained by the different crystal-chemistry of the O' and TOT layers, which commonly present Al^{3+}/Mg^{2+} and Al^{3+}/Si^{4+} substitutions, respectively.

3.4. Phonon dispersion relations.

Phonon dispersion calculations were performed by sampling other **k**-points in the first Brillouin Zone other than Γ (**k** = 0) using a direct-space approach (Dove, 1993; Parlinski et al., 1997; Wallace, 1998). The phonon sampling was conducted on a clinochlore 2 × 2 × 2 supercell constructed from the primitive cell of the mineral.

Phonon dispersion curves of monoclinic clinochlore in the path Γ→Y→M→A→Γ→Y→V→L→Γ is reported in Figure 3 for the 0 – 1200 cm^{-1} range, alongside the calculated total and atom-projected phonon density of states (DOS). The low-frequency region ($\nu < 550$ cm^{-1}) is characterized by magnesium and oxygen vibrations, whereas at higher wavenumbers (750 $cm^{-1} < \nu < 1200$ cm^{-1}) the phonon dispersion is completely dominated by Si – O phonon modes. The spectral region between 550 cm^{-1} and 750 cm^{-1} shows a small contribution from Mg, Si and O atoms to the total DOS, which is mainly due to vibrational motion of hydrogen atoms (projection not showed in the figure for the sake of clarity). As previously discussed, there is a strong anharmonic component in these phonon modes that are not calculated by the CRYSTAL code at the moment. For this reason, this portion of the phonon spectrum has to be considered subject to possible shifts at different wavenumbers.

Acoustic phonon dispersion curves are in adequate agreement with those experimentally measured by inelastic neutron scattering technique by Collins et al. (1993), albeit the poor resolution of the phonon spectra made the comparison difficult.

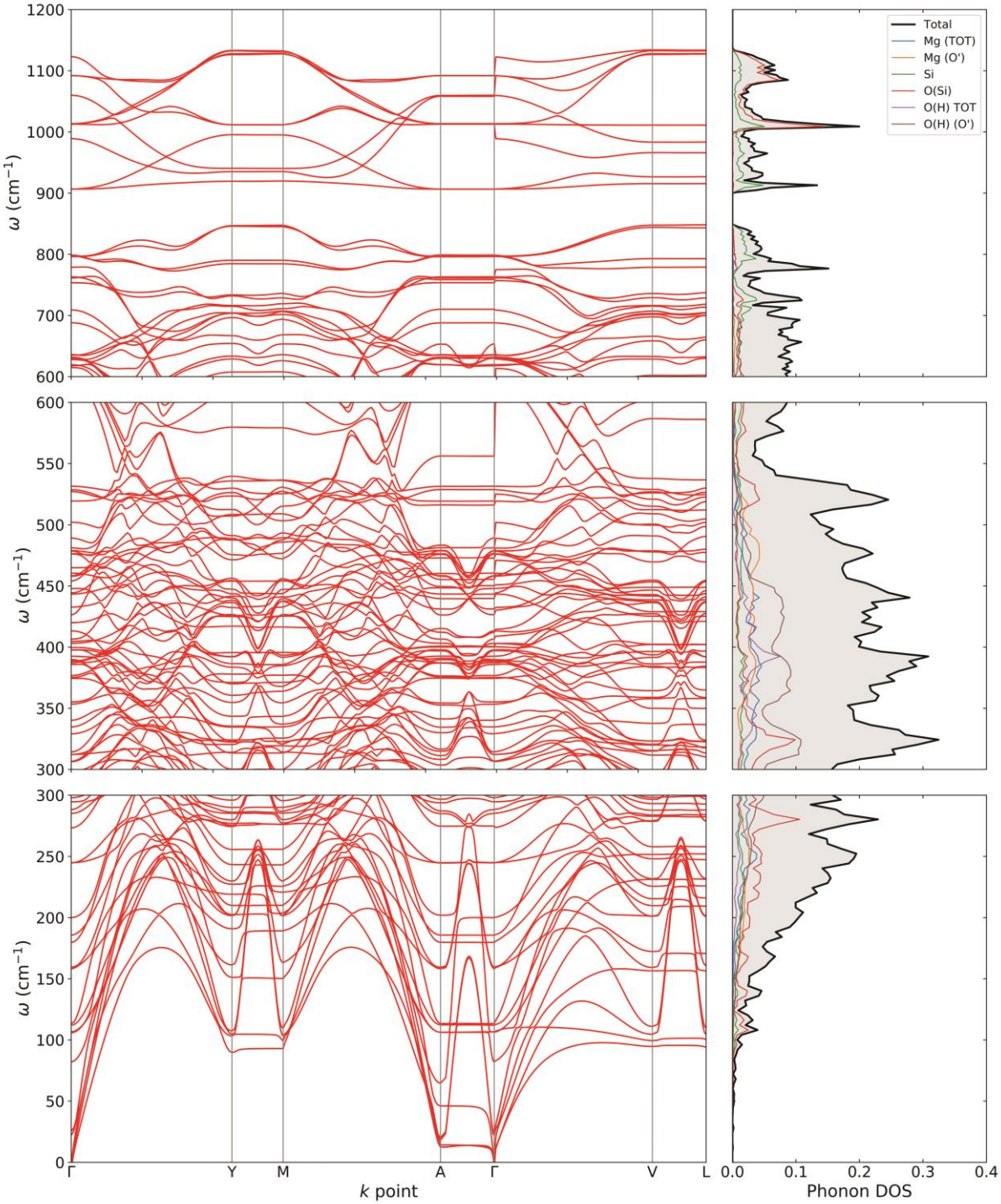

Figure 3. DFT/B3LYP-D* phonon dispersion relations and phonon density of states (DOS) of monoclinic clinochlore (space group *C2/m*) in the frequency range 0 – 1200 cm^{-1}.

As a final note on the phonon properties (Γ-point frequencies and phonon dispersion relations), the authors are aware that clinochlore is typically found with Al^{3+}/Si^{4+} substitutions in both the TOT layer and O' sheet, and other isomorphic substitution may occur in the mineral structure. In general, as reported by several authors (Pawley and Jones, 2011; Ulian et al., 2014; Jollands et al., 2020), crystal-chemical variations from stoichiometric structures can deeply affect the vibrational spectrum. Among the possible effect, it is possible to cite:

(i) increasing number of IR/Raman signals due to lower symmetry of the system (*i.e.*, degeneracy loss of some vibrational modes or activation of silent modes);

(ii) blue or red shifts of the peaks because of the different chemical environment around the vibrating group and/or

(iii) more or less intense signals due to variations of the dipole moment (IR) or polarizability (Raman).

It is possible to extend these considerations to $\mathbf{k} \neq 0$, thus the phonon band structure is more complex and elaborate in a cationic/anionic-substituted mineral phase than that of the end-member term.

However, it was decided to start with the vibrational analysis by considering the simplest clinochlore system, which is the stoichiometric one, a necessary starting point to assign IR/Raman signals to specific vibrations in the structure. Although the system is simple, it represents a novelty because to the authors' knowledge no theoretical information on this subject is present in literature. In addition, Density Functional Theory simulations involving isomorphic substitutions are very demanding from the computational side, in particular for the phonon dispersion relations where supercells are required, and the interpretation of the resulting phonon bands could be a daunting task without those from a reference phase. A comparison between the present theoretical result for the stoichiometric clinochlore and those presenting different kinds and degrees of isomorphic substitutions will be the subject of future works,

which will also aid the assignment of experimental IR/Raman signals to specific vibrational modes in the structure.

4. Conclusions

In this theoretical work, a detailed and accurate analysis of the vibrational properties of monoclinic clinochlore was carried out by means of Density Functional Theory simulations. The results were extensively presented and discussed against the few available experimental findings, with a general good agreement on both the pattern (peak positions and intensities in the IR/Raman spectra) and assignment of the normal modes. The theoretical approach provided further details and extended the knowledge on the vibrational features of this mineral phase, which can be exploited in future studies involving the bulk and the surface of clinochlore.

The small differences between the calculated results and the experimental data in literature are mainly due to the crystal-chemistry of the simulated model. In fact, it was considered an ideal, completely magnesian monoclinic clinochlore without any of the typical substitutions occurring in this mineral, *e.g.* Al^{3+}/Si^{4+} or Al^{3+}/Mg^{2+} in the tetrahedral and O' sites, respectively.

As a final note, the present results showed the relevance of anharmonic OH-modes in both infrared and Raman spectra. While an anharmonic correction was employed in this work for the characterization of the hydroxyl stretching region, at the moment the CRYSTAL code does not calculate the anharmonic contribution for the Mg – O – H (libration) modes.

Acknowledgments

This work is dedicated to the memory of Professor Emilio Galan, who was a world-known scientist, a stimulating collaborator of many works, and a sincere good friend.

Bibliographic references

Balan, E., Saitta, A.M., Mauri, F., Calas, G., 2001. First-principles modeling of the infrared spectrum of kaolinite. Am. Mineral. 86, 1321-1330.

Bayliss, P., 1975. Nomenclature of the trioctahedral chlorites. Can. Mineral. 13, 178-180.

Becke, A.D., 1993. A New Mixing of Hartree-Fock and Local Density-Functional Theories. J. Chem. Phys. 98, 1372-1377, 10.1063/1.464304.

Bhattarai, A., El-Khoury, P.Z., 2019. Nanoscale Chemical Reaction Imaging at the Solid-Liquid Interface via TERS. J. Phys. Chem. Lett. 10, 2817-2822, 10.1021/acs.jpclett.9b00935.

Civalleri, B., Zicovich-Wilson, C.M., Valenzano, L., Ugliengo, P., 2008. B3LYP augmented with an empirical dispersion term (B3LYP-D*) as applied to molecular crystals. CrystEngComm 10, 405-410, 10.1039/b715018k.

Collins, D.R., Stirling, W.G., Catlow, C.R.A., Rowbotham, G., 1993. Determination of acoustic phonon dispersion curves in layer silicates by inelastic neutron scattering and computer simulation techniques. Phys. Chem. Miner. 19, 520-527, 10.1007/BF00203052.

Dominguez, G., Mcleod, A.S., Gainsforth, Z., Kelly, P., Bechtel, H.A., Keilmann, F., Westphal, A., Thiemens, M., Basov, D.N., 2014. Nanoscale infrared spectroscopy as a non-destructive probe of extraterrestrial samples. Nat. Commun. 5, 5445, 10.1038/Ncomms6445.

Dove, M.T., 1993. Introduction to Lattice Dynamics. Cambridge University Press.

Dovesi, R., Erba, A., Orlando, R., Zicovich-Wilson, C.M., Civalleri, B., Maschio, L., Rerat, M., Casassa, S., Baima, J., Salustro, S., Kirtman, B., 2018. Quantum-mechanical condensed matter simulations with CRYSTAL. Wires Comput Mol Sci 8, E1360, 10.1002/Wcms.1360.

Erba, A., Maul, J., Ferrabone, M., Carbonniere, P., Rerat, M., Dovesi, R., 2019a. Anharmonic Vibrational States of Solids from DFT Calculations. Part I: Description of the Potential Energy Surface. J. Chem. Theory Comput. 15, 3755-3765, 10.1021/acs.jctc.9b00293.

Erba, A., Maul, J., Ferrabone, M., Dovesi, R., Rerat, M., Carbonniere, P., 2019b. Anharmonic Vibrational States of Solids from DFT Calculations. Part II: Implementation of the VSCF and VCI Methods. J. Chem. Theory Comput. 15, 3766-3777, 10.1021/acs.jctc.9b00294.

Ferrero, M., Rerat, M., Kirtman, B., Dovesi, R., 2008a. Calculation of first and second static hyperpolarizabilities of one- to three-dimensional periodic compounds. Implementation in the CRYSTAL code. J. Chem. Phys. 129, 244110, 10.1063/1.3043366.

Ferrero, M., Rerat, M., Orlando, R., Dovesi, R., 2008b. The calculation of static polarizabilities of 1-3D periodic compounds. The implementation in the CRYSTAL code. J. Comput. Chem. 29, 1450-1459, 10.1002/jcc.20905.

Firkala, T., Kuschewski, F., Norenberg, T., Klopf, J.M., Pashkin, A., Foerstendorf, H., Rudolph, M., Kehr, S.C., Eng, L.M., 2018. Near-Field Optical Examination of Potassium n-Butyl Xanthate/Chalcopyrite Flotation Products. Minerals-Basel 8, 12, 10.3390/min8030118.

Fries, M., Steele, A., 2018. Raman spectroscopy and confocal raman imaging in mineralogy and petrography, Springer Ser. Surf. Sci. Springer Verlag, pp. 209-236.

Gatti, C., Saunders, V.R., Roetti, C., 1994. Crystal-field effects on the topological properties of the electron-density in molecular-crystals - the case of urea. J. Chem. Phys. 101, 10686-10696, 10.1063/1.467882.

Gopal, N.O., Narasimhulu, K.V., Rao, J.L., 2004. Optical absorption, EPR, infrared and Raman spectral studies of clinochlore mineral. J. Phys. Chem. Solids 65, 1887-1893, 10.1016/j.jpcs.2004.07.003.

Grimme, S., 2006. Semiempirical GGA-type density functional constructed with a long-range dispersion correction. J. Comput. Chem. 27, 1787-1799, 10.1002/jcc.20495.

Jollands, M.C., Blanchard, M., Balan, E., 2020. Structure and theoretical infrared spectra of OH defects in quartz. Eur. J. Mineral. 32, 311-323, 10.5194/ejm-32-311-2020.

King, H.E., Geisler, T., 2018. Tracing mineral reactions using confocal raman spectroscopy. Minerals-Basel 8, 10.3390/min8040158.

Kroumova, E., Aroyo, M.I., Perez-Mato, J.M., Kirov, A., Capillas, C., Ivantchev, S., Wondratschek, H., 2003. Bilbao crystallographic server: Useful databases and tools for phase-transition studies. Phase Transitions 76, 155-170, 10.1080/0141159031000076110.

Kumar, N., Wondergem, C.S., Wain, A.J., Weckhuysen, B.M., 2019. In Situ Nanoscale Investigation of Catalytic Reactions in the Liquid Phase Using Zirconia-Protected Tip-Enhanced Raman Spectroscopy Probes. J. Phys. Chem. Lett. 10, 1669-1675, 10.1021/acs.jpclett.8b02496.

Lafuente, B., Downs, R.T., Yang, H., Stone, N., 2016. The power of databases: The RRUFF project, Highlights in Mineralogical Crystallography. Walter de Gruyter GmbH, Berling, Germany, pp. 1-29.

Lee, C.T., Yang, W.T., Parr, R.G., 1988. Development of the Colle-Salvetti Correlation-Energy Formula into a Functional of the Electron-Density. Phys. Rev. B 37, 785-789, 10.1103/PhysRevB.37.785.

Maschio, L., Kirtman, B., Orlando, R., Rerat, M., 2012. Ab initio analytical infrared intensities for periodic systems through a coupled perturbed Hartree-Fock/Kohn-Sham method. J. Chem. Phys. 137, 204113, 10.1063/1.4767438.

Maschio, L., Kirtman, B., Rerat, M., Orlando, R., Dovesi, R., 2013a. Ab initio analytical Raman intensities for periodic systems through a coupled perturbed Hartree-Fock/Kohn-Sham method in an atomic orbital basis. I. Theory. J. Chem. Phys. 139, 164101, 10.1063/1.4824442.

Maschio, L., Kirtman, B., Rerat, M., Orlando, R., Dovesi, R., 2013b. Ab initio analytical Raman intensities for periodic systems through a coupled perturbed Hartree-Fock/Kohn-Sham method in an atomic orbital basis. II. Validation and comparison with experiments. J. Chem. Phys. 139, 164102, 10.1063/1.4824443.

Momma, K., Izumi, F., 2011. VESTA 3 for three-dimensional visualization of crystal, volumetric and morphology data. J. Appl. Crystallogr. 44, 1272-1276, 10.1107/s0021889811038970.

Monkhorst, H.J., Pack, J.D., 1976. Special points for Brillouin-zone integrations. Phys. Rev. B 8, 5188-5192.

Moro, D., Ulian, G., Valdre, G., 2019a. 3D meso-nanostructures in cleaved and nanolithographed Mg-Al-hydroxysilicate (clinochlore): Topology, crystal-chemistry, and surface properties. Appl. Clay Sci. 169, 74-80, 10.1016/j.clay.2018.12.020.

Moro, D., Ulian, G., Valdrè, G., 2015. Single molecule investigation of glycine-chlorite interaction by cross-correlated scanning probe microscopy and quantum mechanics simulations. Langmuir 31, 4453-4463, 10.1021/acs.langmuir.5b00161.

Moro, D., Ulian, G., Valdrè, G., 2016. Nanoscale cross-correlated AFM, Kelvin probe, elastic modulus and quantum mechanics investigation of clay mineral surfaces: The case of chlorite. Appl. Clay Sci. 131, 175-181, 10.1016/j.clay.2015.11.023.

Moro, D., Ulian, G., Valdrè, G., 2019b. Amino acids-clay interaction at the nano-atomic scale: The L-alanine-chlorite system. Appl. Clay Sci. 172, 28-39, 10.1016/j.clay.2019.02.013.

Nada, R., Nicholas, J.B., McCarthy, M.I., Hess, A.C., 1996. Basis sets for ab initio periodic Hartree-Fock studies of zeolite/adsorbate interactions: He, Ne, and Ar in silica sodalite. Int. J. Quantum Chem. 60, 809-820, 10.1002/(sici)1097-461x(1996)60:4<809::aid-qua3>3.0.co;2-0.

Parlinski, K., Li, Z.Q., Kawazoe, Y., 1997. First-principles determination of the soft mode in cubic ZrO2. Phys. Rev. Lett. 78, 4063-4066, DOI 10.1103/PhysRevLett.78.4063.

Pascale, F., Zicovich-Wilson, C.M., Gejo, F.L., Civalleri, B., Orlando, R., Dovesi, R., 2004. The calculation of the vibrational frequencies of crystalline compounds and its implementation in the CRYSTAL code. J. Comput. Chem. 25, 888-897, Doi 10.1002/Jcc.20019.

Pascale, F., Zicovich-Wilson, C.M., Orlando, R., Roetti, C., Ugliengo, P., Dovesi, R., 2005. Vibration frequencies of $Mg_3Al_2Si_3O_{12}$ pyrope. An ab initio study with the CRYSTAL code. J. Phys. Chem. B 109, 6146-6152, 10.1021/jp050316z.

Pawley, A.R., Jones, R.L., 2011. Hydroxyl stretching in phyllosilicates at high pressures and temperatures: An infrared spectroscopic study. Phys. Chem. Miner. 38, 753-765, 10.1007/s00269-011-0448-x.

Phuakkong, O., Bobuatong, K., Pantu, P., Boekfa, B., Probst, M., Limtrakul, J., 2011. Glycine Peptide Bond Formation Catalyzed by Faujasite. ChemPhysChem 12, 2160-2168, 10.1002/cphc.201100047.

Prencipe, M., Noel, Y., Bruno, M., Dovesi, R., 2009. The vibrational spectrum of lizardite-1T [Mg(3)Si(2)O(5)(OH)(4)] at the Gamma point: A contribution from an ab initio periodic B3LYP calculation. Am. Mineral. 94, 986-994.

Prencipe, M., Pascale, F., Zicovich-Wilson, C.M., Saunders, V.R., Orlando, R., Dovesi, R., 2004. The vibrational spectrum of calcite (CaCO3): an ab initio quantum-mechanical calculation. Phys. Chem. Miner. 31, 559-564, DOI 10.1007/s00269-004-0418-7.

Rinaudo, C., Roz, M., Boero, V., Franchini-Angela, M., 2004. FT-Raman spectroscopy on several di- and tri-octahedral T-O-T phyllosilicates. Neues Jb Miner Monat, 537-554, 10.1127/0028-3649/2004/2004-0537.

Rosso, K.M., Bodnar, R.J., 1995. Microthermometric and Raman-spectroscopic detection limits of CO_2 in fluid inclusions and the Raman-spectroscopic characterization of CO_2. Geochim. Cosmochim. Acta 59, 3961-3975, Doi 10.1016/0016-7037(95)94441-H.

Stueckenschneider, K., Merz, J., Schembecker, G., 2014. Molecular Interaction of Amino Acids with Acidic Zeolite BEA: The Effect of Water. J. Phys. Chem. C 118, 5810-5819, 10.1021/jp411734j.

Tosoni, S., Pascale, F., Ugliengo, P., Orlando, R., Saunders, V.R., Dovesi, R., 2005. Quantum mechanical calculation of the OH vibrational frequency in crystalline solids. Mol. Phys. 103, 2549-2558, 10.1080/00268970500180808.

Ugliengo, P., Viterbo, D., Chiari, G., 1993. MOLDRAW: molecular graphic on a personal computer. Z. Kristallogr. 207, 9-23, 10.1524/zkri.1993.207.Part-1.9.

Ulian, G., Moro, D., Valdrè, G., 2016. First-principles study of structural and surface properties of (001) and (010) surfaces of hydroxylapatite and carbonated hydroxylapatite. J. Appl. Crystallogr. 49, 1893–1903, 10.1107/S160057671601390X.

Ulian, G., Moro, D., Valdrè, G., 2018. First principle investigation of the mechanical properties of natural layered nanocomposite: Clinochlore as a model system for heterodesmic structures. Composite Structures 202, 551-558, 10.1016/j.compstruct.2018.02.089.

Ulian, G., Valdrè, G., 2015. Density functional investigation of the thermo-physical and thermo-chemical properties of 2M(1) muscovite. Am. Mineral. 100, 935-944, 10.2138/am-2015-5086.

Ulian, G., Valdrè, G., Corno, M., Ugliengo, P., 2014. DFT investigation of structural and vibrational properties of type B and mixed A-B carbonated hydroxylapatite. Am. Mineral. 99, 117-127, 10.2138/am.2014.4542.

Valdrè, G., 2007. Natural nanoscale surface potential of clinochlore and its ability to align nucleotides and drive DNA conformational change. Eur. J. Mineral. 19, 309-319, Doi 10.1127/0935-1221/2007/0019-1732.

Valdrè, G., Malferrari, D., Brigatti, M.F., 2009. Crystallographic Features and Cleavage Nanomorphology of Chlinochlore: Specific Applications. Clays Clay Miner. 57, 183-193, 10.1346/Ccmn.2009.0570205.

Valdrè, G., Moro, D., Hounsome, C.M., Antognozzi, M., 2012. SPM nanolithography of hydroxy-silicates. Nanotechnology 23, 85301-85301, 10.1088/0957-4484/23/38/385301.

Valdrè, G., Moro, D., Ulian, G., 2011a. Interaction of organic molecules with layer silicates, oxides and hydroxides and related surface-nano-characterization techniques, in: Brigatti, M.F., Mottana, A. (Eds.), Layered Mineral Structures and Their Application in Advanced Technologies, pp. 313-334.

Valdrè, G., Moro, D., Ulian, G., 2011b. Nucleotides, RNA and DNA selective adsorption on atomic-flat Mg-Al-hydroxysilicate substrates. Micro & Nano Letters 6, 922-926, 10.1049/mnl.2011.0546.

Valdrè, G., Tosoni, S., Moro, D., 2011c. Zeolitic-type 'Bronsted-Lowry sites distribution imaged on clinochlore. Am. Mineral. 96, 1461-1466, 10.2138/am.2011.3774.

Valenzano, L., Torres, F.J., Klaus, D., Pascale, F., Zicovich-Wilson, C.M., Dovesi, R., 2006. Ab initio study of the vibrational spectrum and related properties of crystalline compounds; the case of $CaCO_3$ calcite. Z. Phys. Chem. 220, 893-912, 10.1524/zpch.2006.220.7.893.

Wallace, D.W., 1998. Thermodynamics of Crystals. Dover Publications.

Welch, M.D., Marshall, W.G., 2001. High-pressure behavior of clinochlore. Am. Mineral. 86, 1380-1386.

Wiewiora, A., 1990. Crystallochemical Classifications of Phyllosilicates Based on the Unified System of Projection of Chemical-Composition .3. The Serpentine-Kaolin Group. Clay Miner. 25, 93-98, DOI 10.1180/claymin.1990.025.1.10.